Research Article

ADVANCED PHOTONICS

# Tunable lasing direction in one-dimensional suspended high-contrast grating using bound states in the continuum

Zhen-Ting Huang,[a] Chiao-Yun Chang,[a] Kuo-Ping Chen,[b,c] and Tien-Chang Lu[a,*]
[a]National Yang Ming Chiao Tung University, College of Electrical and Computer Engineering, Department of Photonics, Hsinchu, Taiwan
[b]National Tsing Hua University, Institute of Photonics Technologies, Hsinchu, Taiwan
[c]National Yang Ming Chiao Tung University, Institute of Imaging and Biomedical Photonics, Tainan, Taiwan

**Abstract.** We realized off-Γ lasing using the Friedrich–Wintgen bound state in the continuum (FW-BIC) in a one-dimensional suspended high-contrast grating (HCG). A clear anticrossing was observed in the band diagram of the HCG corresponding to the coupling between the specific different orders of Bloch modes, and the FW-BIC with a high quality factor and large confinement factor was observed near the anticrossing point. Owing to these outstanding characteristics, the FW-BIC can serve as a robust and extraordinary cavity mode for realizing low-threshold laser operation and for achieving angle-steering laser beams. The conditions of the FW-BIC can be modulated by tuning the geometry related to the coupling modes in the anticrossing, resulting in a tunable lasing direction observed in the measurement. Furthermore, through appropriate design, the emission angle can be controlled precisely within a wide tunable range. Therefore, FW-BICs can be used to realize high-resolution directional lasing within a wide range of emission angles; they can also be applied in three-dimensional sensing for lidar applications.

Keywords: bound state in the continuum; Friedrich–Wintgen bound state in the continuum; strong coupling; anticrossing; beam steering.

Received Aug. 5, 2022; revised manuscript received Nov. 7, 2022; accepted for publication Nov. 29, 2022; published online Dec. 30, 2022.



[DOI: 10.1117/1.AP.4.6.066004]

## 1 Introduction

Bound state in the continuum (BIC) is an intriguing eigenstate which exists in the continuous spectrum, has an infinite lifetime, and does not couple with any other radiation state.[1,2] This wave phenomenon was first proposed by von Neumann and Wigner;[3] it was derived from the Schrödinger equation and describes a localized electronic eigenstate in a particular potential. Recently, BICs in photonic systems have been extensively used. A state with a theoretically infinite quality ($Q$) factor is highly effective in improving the performance of optical devices. Thus, photonic BICs are used in various applications, including in optical sensors with extraordinary sensitivity,[4] optical antennas for light manipulation,[5,6] and laser cavities with ultralow lasing threshold.[7–10] Owing to the characteristics of BICs, those states should be operated inside the light cone.[1,11] Therefore, photonic BICs are commonly formed according to the periodic structure. The Bloch theorem holds that the periodic lattice supports lattice momentum, which can shift optical modes from each higher-order Brillouin zone to the first Brillouin zone and can then make them fall into the light cone.[12] Furthermore, because of the periodic potential, the mode at the Γ point is split into two band-edge modes, which contain even and odd phases in the near field and open a complete bandgap. In a one-dimensional (1D) system, the even phase corresponds to the bright mode, which induces constructive interference in the far field and forms extra radiation channels. Therefore, because of excess leakage in this mode, sustaining sufficient light–matter interaction during laser operation is challenging. By contrast, the odd phase corresponds to the dark mode, and the destructive interference in the far field causes the phase to strongly confine the optical field within the structure, thus forming a bounded optical

*Address all correspondence to Tien-Chang Lu, timtclu@nycu.edu.tw

state with an ultrahigh $Q$ factor. The odd mode is also referred to as the symmetry-protected BIC.[11,13,14] Owing to its high $Q$ factor, the mode can be used to design a low-threshold BIC laser, and the emission angle is fixed to the normal direction because this mode should be operated at the Γ point.

Photonic BICs can also be produced through anticrossing coupling.[1,2,15,16] According to the coupled oscillator model, if two states are present in a coupled system and the real component of their energy detuning is zero, strong coupling occurs because of sufficiently large coupling strength.[17] Subsequently, the original states are split into two states and separated by a local bandgap, and particularly, an anticrossing is observed in their dispersions. Because of this strong coupling, a bounded state formed through destructive interference in the far field is observed at a particular position of the anticrossing bands. Compared with the symmetry-protected BIC, this bounded state is not limited to any high-symmetry point but is only related to the coupling strength and has an ultrahigh $Q$ factor. Therefore, off-Γ laser operation can be easily realized and exhibits a higher degree of freedom, which can be used to design a laser with multidirectional lasing characteristics. Such a bound state involving the coupling of two states is referred to as the Friedrich–Wintgen BIC (FW-BIC). The conditions of anticrossing can be modulated by tuning the coupling component or coupling strength, leading to a shift of the FW-BIC. This characteristic of FW-BICs aids in the design of a laser cavity with beam-steering capability.

Owing to the remarkable properties of BIC, it can be used as a laser cavity mode to realize directional lasing. In 2018, Ha *et al.*[18] used a GaAs nanopillar array with a rectangular lattice to design a quasi-BIC laser with off-Γ lasing characteristics. The symmetry-protected BIC constituted by the resonance of the vertical electric dipole had an ultrahigh $Q$ factor at the Γ point. The tuning of one of the periods in the rectangular lattice resulted in the intersection of an additional leaky band with the symmetry-protected BIC at two crossing points in the off-Γ region, thus forming additional radiation channels and promoting quasi-BIC lasing in the off-normal direction. Some directional off-Γ lasing has also been experimentally demonstrated and realized through a similar design mechanism.[19,20] These lasers are all primarily operated in the quasi-BIC rather than in the BIC. Although these designs can be used to realize off-Γ lasing, the emission angles only slightly deviate from 0 deg, and shifting them to a larger angle is difficult because the quasi-BIC must be close to the BIC. Therefore, to increase practical applicability, a robust design with a wide range of tunability is necessary for laser applications.

In this study, a 1D suspended high-contrast grating (HCG) was applied to design an off-Γ FW-BIC laser with directional lasing characteristics and a precisely controllable emission angle. The formation of the FW-BIC can be regarded as the coupling of different orders of Bloch modes. Notably, the degree of freedom of higher-order solutions corresponds to the thickness of the HCG. To determine the exact coupling mode of the FW-BIC, the band intersection between several orders of Bloch modes is first calculated, and the sufficiency of the coupling strength for inducing an anticrossing in the band diagram is then determined. Once anticrossing is observed, the coupling mode can be determined, and the strong coupling condition can be realized. Therefore, by utilizing this condition, we can design an anticrossing within the gain spectrum in the band diagram. Moreover, the FW-BIC, which is close to the anticrossing point and has a locally high $Q$ factor, can be designed as the cavity mode to enable low-threshold lasing and off-Γ operation. Additionally, by conveniently tuning the geometry of the HCG, the band intersection of the coupling modes can be modulated, which changes the position of the anticrossing and the FW-BIC and results in a steerable lasing characteristic. Compared with the previously demonstrated accidental BICs,[15,21–23] the appearance of the FW-BIC proposed in this study can be controlled more precisely, resulting in the wide-range tunability of the emission angle in the FW-BIC laser. This extraordinary property induces beam-steering capability in the 1D suspended HCG, making it suitable for lidar applications in the future.

## 2 Results and Discussion

To explore the formation of the FW-BIC, the Bloch mode and its band diagram were first designed using a unit cell of a suspended HCG, as shown in Fig. 3(d). The suspended HCG was composed of GaAs with eight pairs of InGaAs multiple quantum wells (MQWs) and was surrounded by air. The simulation focused only on the transverse electric (TE)-polarized solution, which matched the preferred gain mode of MQWs corresponding to compressive strain. The photoluminescence (PL) spectrum of this InGaAs/GaAs epitaxial wafer is depicted in Fig. S2 in the Supplementary Material; a gain peak was observed at 937 nm in the PL spectrum. Notably, with the coupling of the periodic lattice, band-edge modes separated by the complete bandgap comprised the even and odd phases at the Γ point. Because of the difference in energy confinement, the difference in the effective index between the even and odd modes varied with the increase in the thickness of the HCG ($h$), thereby resulting in an unequal wavelength shift, as observed in the band diagram. Therefore, band intersection between different orders of Bloch modes was achieved by tuning the thickness of HCG. Figure 1 shows the band diagram of the HCG with the lattice constant ($a$) and filling factor (FF) fixed at 423 nm and 0.65, respectively; the ratio of $h/a$ changed to 0.65, 1, and 1.65. The band intersections between the fundamental even mode and first-order, second-order, and third-order odd modes are shown in Figs. 1(a), 1(b), and 1(c), respectively, wherein the lower panels depict the corresponding mode profiles at the Γ point. An anticrossing was observed when the fundamental even mode intersected with the second-order odd mode, and the other modes only exhibited a crossing point in the band diagram. This distinct difference could be attributed to the coupling strength of the intersected modes and was caused by the overlap of mode profiles (see Supplementary Material). As displayed in the overlap integral in Fig. S1 in the Supplementary Material, the fundamental even mode and second-order odd mode exhibited the largest overlap in electric-field distribution, resulting in sufficiently strong coupling strength for producing an anticrossing in the off-Γ region.

The FW-BIC was observed near the anticrossing point. To make the FW-BIC closer to the emission band of MQWs, the thickness of the HCG was fixed at 423 nm, and the lattice constant and FF were slightly adjusted to 427 nm and 0.674, respectively; the corresponding band diagram is shown in Fig. 2(a). By calculating the $Q$ factor, a striking $Q$ peak was observed at 34 deg in the lower band in Fig. 2(c), which was close to the anticrossing point in the band diagram. This local $Q$ peak corresponded to the formation of the FW-BIC, and its wavelength was calculated to be 940 nm according to the dispersion illustrated in Fig. 2(a). In addition to the FW-BIC,

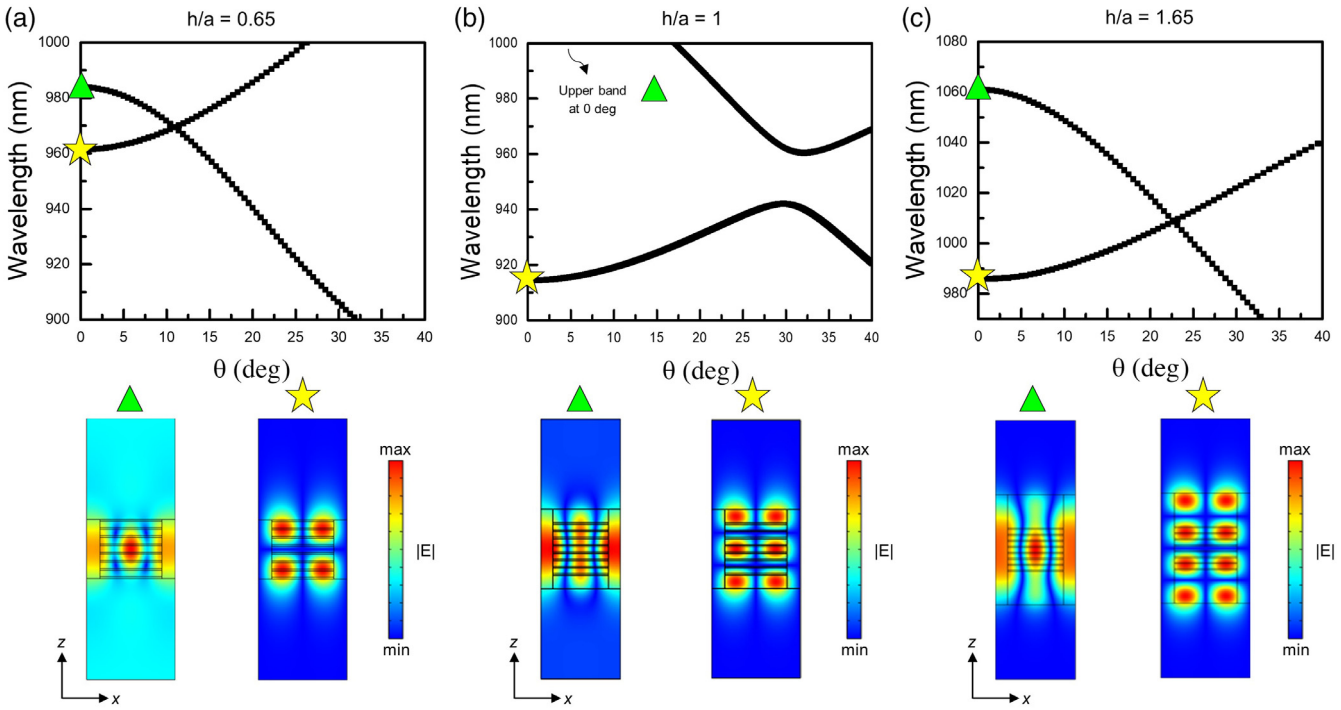


**Fig. 1** Mode dispersion between different orders of Bloch modes. (a) Band intersection between the fundamental even mode (triangular) and first-order odd mode (star) when the thickness and lattice constant ratio ($h/a$) was 0.65; (b) band intersection between the fundamental even mode (triangular) and second-order odd mode (star) when the $h/a$ ratio was 1; (c) band intersection between the fundamental even mode (triangular) and third-order odd mode (star) when the $h/a$ ratio was 1.65. The lower panels depict the corresponding electric-field distribution of the triangular and star point indicated by the Γ point in the band diagram.

a steep $Q$ peak with a value considerably higher than that of the FW-BIC was observed at 0 deg in the lower band. The peak with a higher $Q$ factor was observed corresponding to the band-edge of the second-order odd mode, which corresponded to the dark mode at the Γ point. To prevent the competition of this mode with the FW-BIC for gain from MQWs, the wavelength of the symmetry-protected BIC was designed to be 13 nm away from the gain peak. Furthermore, because of the strong coupling, the lower band transformed from the second-order odd mode in the left band to the fundamental even mode in the right band, separated by the anticrossing point. According to the location of the $Q$ peaks, the FW-BIC was in the right part of the lower band, indicating that its characteristics were closer to the fundamental even mode than to the second-order odd mode. This characteristic was also observed in the electric-field distribution of the orange diamond, which comprised the same even phase as that of the fundamental even mode, as shown in Fig. 2(b). Additionally, the MQW confinement factor ($\Gamma_{QW}$) of the upper and lower bands was calculated using the eigenvalue solver and frequency-domain solver shown in Figs. 2(d) and 2(e), respectively. Because the confinement factor of the fundamental even mode was larger than that of the second-order odd mode, the FW-BIC also had a large confinement factor for MQWs, which was ∼15.52%, as shown in Fig. 2(d). In Fig. 2(e), the FW-BIC was observed where the linewidth suddenly and dramatically shrank, meaning that the FW-BIC had a high $Q$ factor and a large confinement factor. Owing to these characteristics, the FW-BIC can be used to design the laser cavity mode and realize low-threshold lasing and off-Γ operation.

Figure 3(a) shows the schematic of the off-Γ FW-BIC laser with a 1D suspended HCG. The grating structure was fabricated through electron beam lithography and inductively coupled plasma dry etching. The suspended membrane was fabricated through wet etching, wherein a sacrificial layer of $Al_xGa_{1-x}As$ was etched by immersing the sample into the buffered oxide etchant (BOE), which was mixed with hydrofluoric acid (HF) and ammonium fluoride ($NH_4F$) at a mixing ratio of 1:6. Furthermore, the 1D suspended HCG was fabricated through a careful drying process. The period, FF, and thicknesses of the HCG were selected as 427, 0.674, and 423 nm, respectively. Figure 3(b) shows the corresponding scanning electron microscope (SEM) image, wherein the rectangular windows enclosed around the HCG-enabled uniform etching of the sacrificial layer using the BOE. Figures 3(c) and 3(d) show the schematics of the cross section and unit cell of the suspended HCG, respectively; the thicknesses of the InGaAs QW and GaAs barrier were 8 and 30 nm, respectively. To measure the etched depth after the wet-etching process, the focus ion beam (FIB) was used to cut the cross section of the HCG, as shown in Fig. 3(e). Subsequently, the etched depth was determined, which was ∼400 nm after immersion in BOE for 3 min. This etching depth confined the optical mode to the suspended HCG film, which was not coupled with the underlying layers.

After the sample was prepared, optical pumping was performed at room temperature using a 532-nm pulse laser with

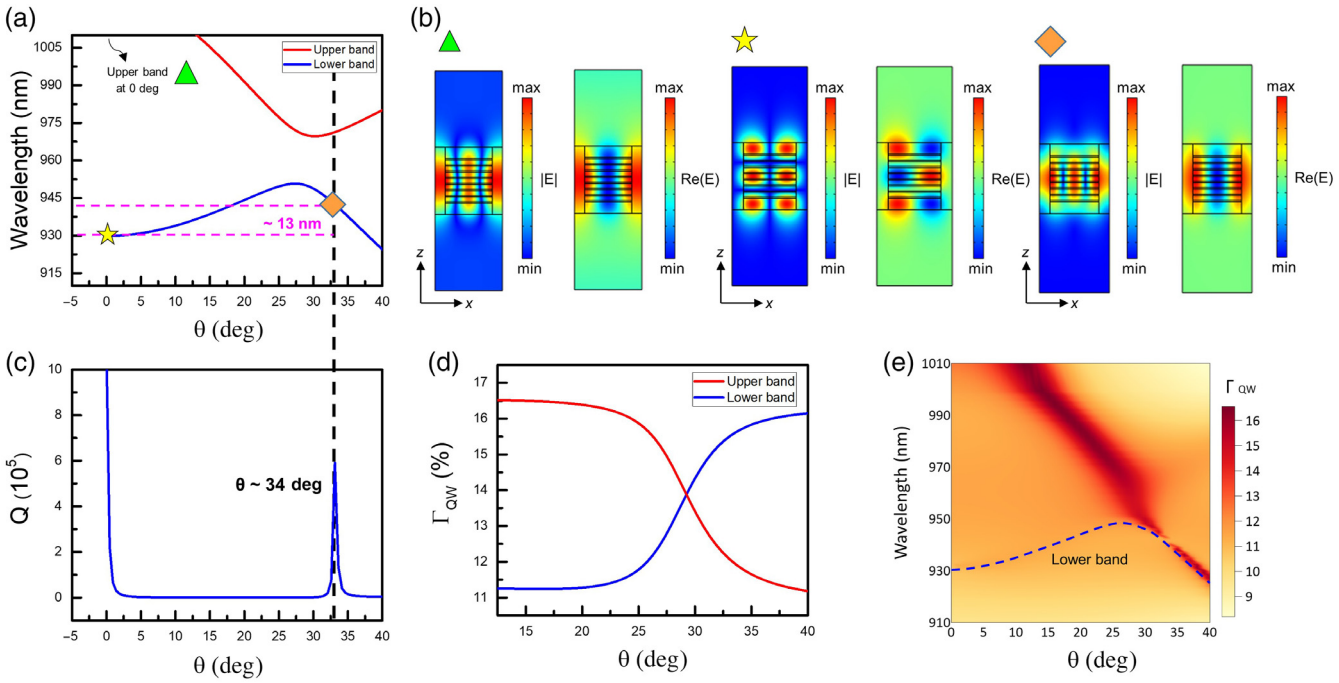


**Fig. 2** Formation of off-Γ FW-BIC and its characteristics. (a) Band diagram of a 1D suspended HCG, whose period, FF, and thickness were 427, 0.674, and 423 nm, respectively. The diamond point indicates the position of the off-Γ FW-BIC. (b) Electric-field distribution of the fundamental even mode, second-order odd mode, and the FW-BIC, which is indicated as the triangular, star, and diamond point in (a), respectively; (c) $Q$ value as a function of the off-angle of the lower band; (d) confinement factors of the upper and lower bands as a function of the off-angle; (e) confinement factor map as a function of the wavelength and the off-angle of the incident light.

a repetition frequency of 1 kHz and a pulse duration of 0.35 ns; the angle-resolved PL (ARPL) maps below and above the lasing threshold are displayed in Figs. 4(a) and 4(b), respectively. A prominent lasing peak was observed at 941 nm, and the emission angle was 34 deg, which was consistent with the simulation results displayed in Fig. 2. Compared with the observed band, the simulated lower band indicated by the dotted line and its $Q$ values calculated as a function of the off-angle are separately shown in Figs. 4(a) and 4(d). As shown in Fig. 4(a), the left part of the observed band disappeared, but the right part was clear and fitted well with the simulated band because the left and right parts of the lower band corresponded to different modes before coupling, and the notable difference in their confinement factors corresponded to the different emission characteristics of the two parts. The disappearance of the left part of the band could be attributed to the low-MQW confinement factor of the second-order odd mode. Figures 4(c), 4(e), and 4(f) display the light-in versus light-out (L-L) curve, far-field polarization, and power-dependent PL spectra, respectively. The lasing threshold was ~37.6 $\mu$W, and the linewidth was 6.7 nm. The relatively large linewidth could be attributed to the random reflection and scattering of light from the unevenly etched surface of the sacrificial layer. The measured far-field polarization was perpendicular to the periodic direction of the HCG, corresponding to TE polarization. The measured polarization was identical to that obtained through simulation, and the degree of polarization was as high as 82.8%. The results indicated that the lasing behaviors of the FW-BIC were effective for the off-Γ operation. Through the proposed coupling between two conventional modes in the suspended HCG, a robust bound state with an extraordinary $Q$ factor and optical confinement can be obtained. Furthermore, by tuning the coupling modes and shifting the anticrossing point, this state can be easily modulated and can thus be used to realize beam steering.

To verify the tunability of the FW-BIC, the FF of the HCG was changed to 0.64, 0.65, 0.72, and 0.74; the corresponding band diagram and $Q$ factors are displayed in Fig. 5. The changes in the FF led to a shift of the anticrossing point; thus, the FW-BIC shifted to another angle. Moreover, to ensure that the wavelength of the FW-BIC was close to the PL peak of MQWs, the lattice constant of the HCG was set to 443, 432, 410, and 408 nm, as illustrated in Figs. 5(a), 5(b), 5(c), and 5(d), respectively. These band diagrams indicated that with the increase in the FF, the angle of the anticrossing point increased because of the shift of the band intersection between the fundamental even mode and second-order odd mode. Similarly, according to the $Q$ factor of the lower band shown in Figs. 5(e)–5(h), the angle of the local $Q$ peak gradually deviated from the normal direction and shifted from 26 deg to 38 deg. Owing to such a wide tunable range of operating angles, the FW-BIC exhibited a flexible structural design and was effective in realizing beam steering. Furthermore, the symmetry-protected BIC was based on the 1D suspended HCG, as shown in Fig. S3 in the Supplementary Material. The band displayed in Fig. S3(a) in the Supplementary Material corresponds to the fundamental odd mode, which is the dark mode at the Γ point and has an ultrahigh $Q$ factor, and its period and FF are 289 and 0.692 nm, respectively.

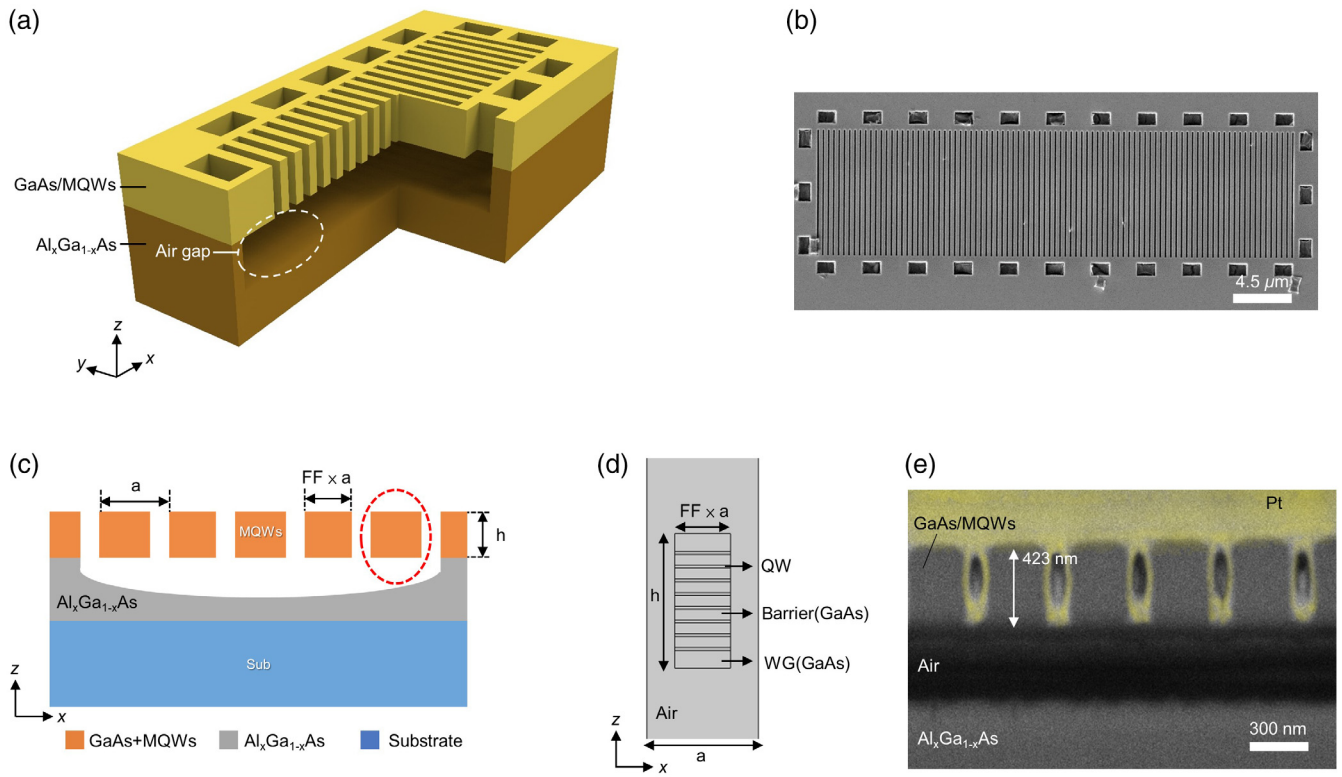


**Fig. 3** Fabrication of the 1D suspended HCG. (a) Schematic and (b) SEM image of the top-view of the 1D suspended HCG. (c) Schematic of the cross section, where the orange, gray, and blue parts depict the HCG with eight pairs of MQWs, the sacrificial layer of $Al_xGa_{1-x}As$, and GaAs substrate, respectively. (d) Simulated unit cell of the HCG; the thickness of each QW, barrier, and waveguide (WG) layer was 8, 30, and 74.5 nm, respectively; (e) cross-sectional SEM image of the suspended HCG etched by the FIB. The etching depth was ~400 nm.

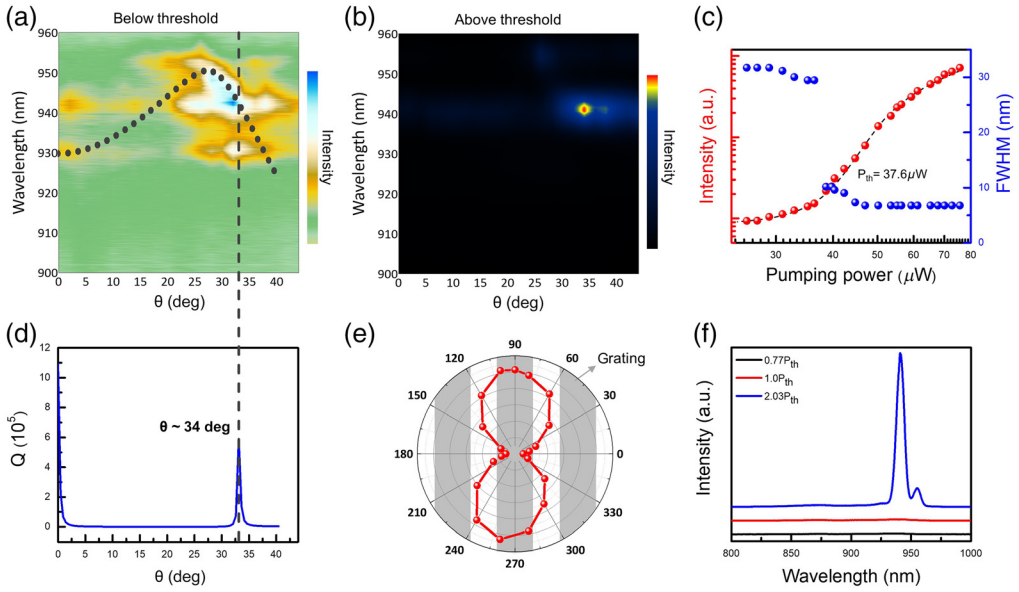


**Fig. 4** Directional lasing characteristics of the FW-BIC in the 1D suspended HCG. The ARPL maps (a) below and (b) above the lasing threshold. The dotted line in (a) indicates the simulated lower band displayed in Fig. 2(a). (c) L-L curve of the 1D suspended HCG, and the lasing threshold was ~37.6 $\mu$W. (d) $Q$ values of the simulated lower band as a function of the off-angle; (e) far-field polarization and (f) power-dependent PL spectra of the 1D suspended HCG.

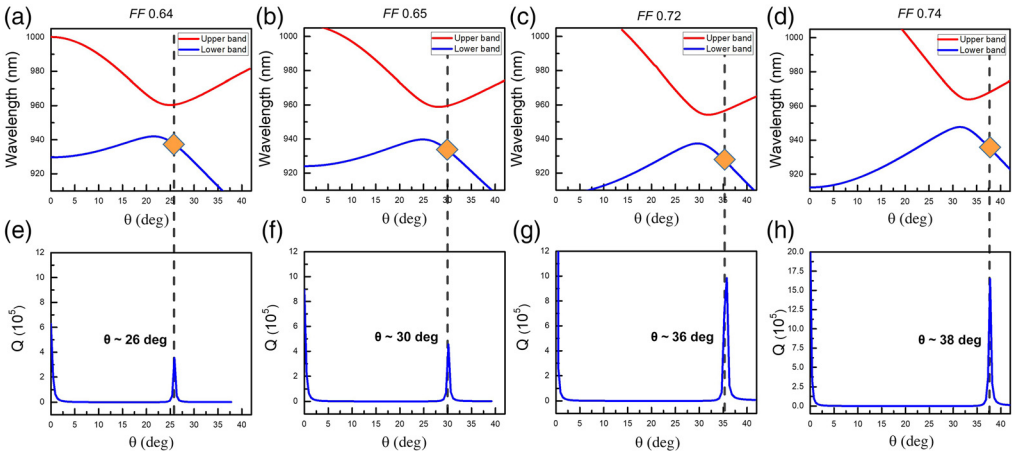


**Fig. 5** Design of tunable FW-BIC bands. (a)–(d) Band diagrams of 1D suspended HCGs with FFs designed to be 0.64, 0.65, 0.72, and 0.74, respectively; the lattice constants were separately tuned to 443, 432, 410, and 408 nm to shift the wavelength of the FW-BIC close to that of the PL peak of MQWs. (e)–(h) $Q$ values of the lower bands as functions of off-angles, with local peaks located at 26 deg, 30 deg, 36 deg, and 38 deg, respectively.

Based on the aforementioned designs, 1D suspended HCGs were fabricated for different emission angles, and their detailed size and measurement results are shown in Fig. S4–S8 in the Supplementary Material. Figure 6(a) displays the ARPL maps of the suspended HCGs above the lasing threshold. Lasing peaks were observed in the spectra at different emission angles (0 deg, 26 deg, 30 deg, 34 deg, 36 deg, and 40 deg from top to bottom). The lasing peak at 0 deg in the suspended HCG corresponded to the symmetry-protected BIC, and the others corresponded to the FW-BICs. Additionally, Fig. 6(b) shows the simulated geometric condition for the multiangle operation of the FW-BIC. The position of the FW-BIC could be easily modulated by a selected geometry; therefore, multiangle lasing can be realized in FW-BIC lasers, as indicated by the measurement results displayed in Fig. 6(a). Based on these results, directional lasing can be achieved in the 1D suspended HCG, and the corresponding emission angle can be easily modulated by operating on the FW-BIC and tuning the geometry related to the anticrossing coupling. Furthermore, owing to the tunability of the lasing direction, FW-BIC laser arrays can be designed to realize wide-range multiangle lasing, whose schematic is illustrated in Fig. 6(b). Unlike in other proposed beam-steering designs, lasing in the laser cavity is required to couple with a passive optical component, such as metasurfaces, to modulate the emission angle[24–27]; therefore, the output power is attenuated owing to its coupling efficiency. By contrast, FW-BIC lasers, which are active optical components with beam-steering capability, exhibit stronger potential for realizing large-scale and high-resolution laser scanning and can be used in lidar applications.

## 3 Conclusion

We designed an off-Γ FW-BIC laser based on the anticrossing coupling in a 1D suspended HCG. Band intersections were induced between different orders of Bloch modes to design two modes with sufficiently high coupling strength to achieve anticrossing. According to the simulation results, when the fundamental even mode intersected with the second-order odd mode, a clear anticrossing, corresponding to a large overlap in electric-field distribution, was observed in the band diagram. Moreover, a local $Q$ peak was observed near the anticrossing point and was far from the Γ point, corresponding to the construction of the FW-BIC. The FW-BIC was located in the right part of the lower band of the anticrossing; it not only had a high $Q$ factor but also a large confinement factor in the fundamental even mode, making the FW-BIC suitable to be applied in the laser cavity. Subsequently, we fabricated a 1D HCG based on the simulation with an FF of 0.674 and used a wet-etching process to make it suspended. After optical pumping, a prominent lasing peak was observed at 941 nm, and the emission angle was 34 deg, which matched the simulated position of the FW-BIC. Furthermore, the measured optical band was consistent with that obtained through the simulation, but the left part disappeared because of its low MQW confinement factor. Moreover, the FW-BIC accompanied by the anticrossing can be modulated by varying the FF, which is related to the band intersection between the fundamental even mode and second-order odd mode; the resulting off-Γ FW-BIC laser possesses a tunable lasing direction. Furthermore, we fabricated 1D suspended HCGs with different filing factors (0.64, 0.65, 0.72, and 0.74). We also fabricated a suspended HCG operating on the symmetry-protected BIC. Through optical measurement, directional lasing was observed at 0 deg, 26 deg, 30 deg, 36 deg, and 40 deg, indicating the tunability of the FW-BIC. Moreover, these results indicated the robustness of the coupling mechanism for fabricating FW-BICs; the mechanism can thus be used to achieve beam steering. Owing to these remarkable characteristics, FW-BIC laser arrays with wide-range multiangle lasing can be used to realize high-resolution three-dimensional sensing and in lidar applications.

## 4 Appendix: Experimental Section

### *4.1 ARPL Measurement Setup*

ARPL measurement was performed using a 532-nm pulse laser with a repetition rate of 1 kHz, a pulse duration of 0.35 ns, and an obliquely incident angle of ∼40 deg. The angle-resolved

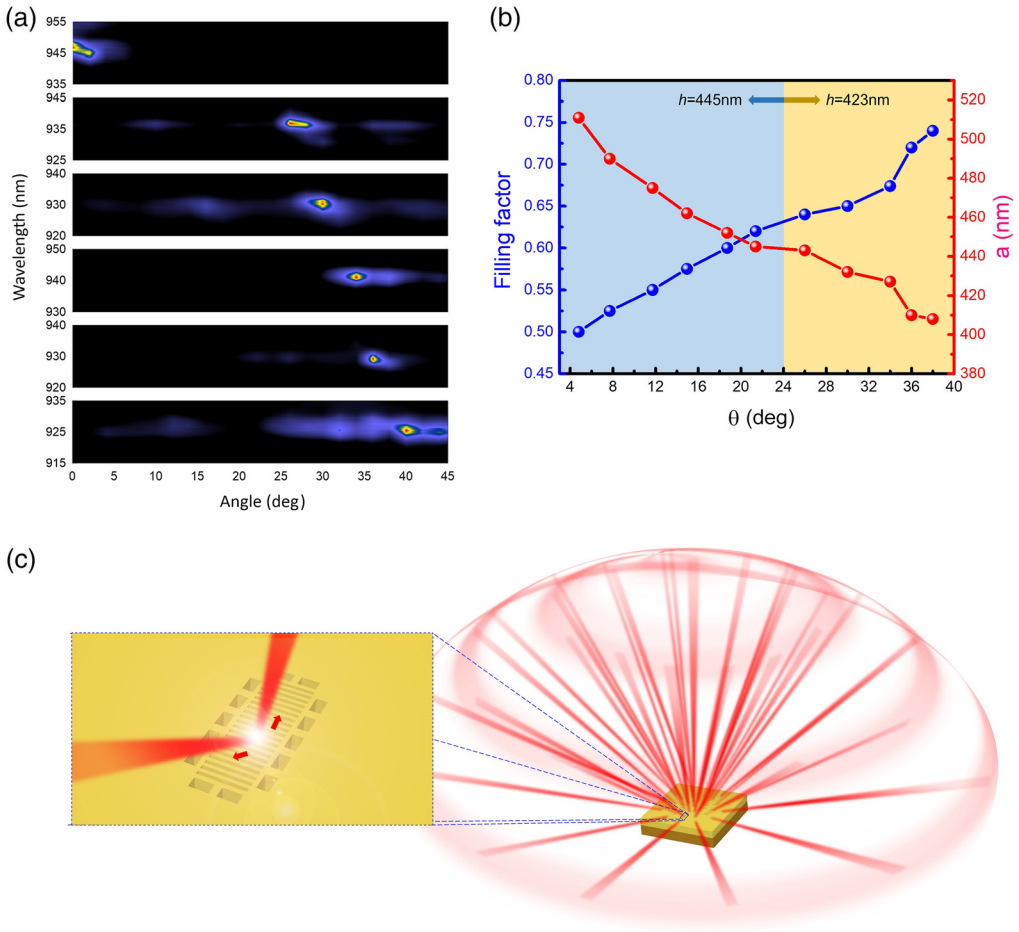


**Fig. 6** Realization of the tunable lasing direction in the 1D suspended HCG. (a) ARPL maps above the lasing threshold; the lasing angle included 0 deg, 26 deg, 30 deg, 34 deg, 36 deg, and 40 deg from top to bottom. The 0 deg lasing angle was obtained using the symmetry-protected BIC, and the other lasing angles were obtained using the FW-BIC. (b) Simulated geometric parameters of FW-BICs; $\theta$ is determined by the peak position of the $Q$ factor of the FW-BIC, and their wavelength was tuned to near the PL peak of MQWs. Using the proposed design method, $\theta$ can be controlled precisely, indicating that the FW-BIC provides wide-range tunability and facilitates multi-angle lasing. (c) Schematic of the FW-BIC laser array constituting a wide-range multi-angle lasing.

lasing signal was collected using a near-infrared optical fiber with a 600-$\mu$m core mounted on a rotating stage, which had an angular resolution of 1 deg. The lasing signal was detected using a nitrogen-cooled charge-coupled device attached to the monochromator.

### 4.2 Simulations of Laser Characteristics

All the simulations were performed using an eigenfrequency and a frequency-domain solver in the finite-element software COMSOL Multiphysics.

## Acknowledgments

We thank Prof. Tzy-Rong Lin of National Taiwan Ocean University and Prof. Chan-Shan Yang of National Taiwan Normal University for their contributions to our discussion. This study was financially supported by Taiwan's Ministry of Science and Technology under contract number MOST 110-2221-E-A49-058-MY3.

## References

1. C. W. Hsu et al., "Bound states in the continuum," *Nat. Rev. Mater.* **4**, 16048 (2016).
2. K. Koshelev et al., "Nonradiating photonics with resonant dielectric nanostructures," *Nanophotonics* **8**, 725–745 (2019).
3. J. von Neumann and E. P. Wigner, "Über merkwürdige diskrete Eigenwerte," *Phys. Z.* **30**, 465–467 (1929).
4. H. Zhang et al., "Quasi-BIC laser enabled by high-contrast grating resonator for gas detection," *Nanophotonics* **11**, 297–304 (2022).
5. H. Xu and Y. Shi, "Diffraction engineering for silicon waveguide grating antenna by harnessing bound state in the continuum," *Nanophotonics* **9**, 1439–1446 (2020).
6. Z. Han et al., "Significantly enhanced second-harmonic generations with all-dielectric antenna array working in the quasi-bound states in the continuum and excited by linearly polarized plane waves," *Nanophotonics* **10**, 1189–1196 (2021).
7. A. Kodigala et al., "Lasing action from photonic bound states in continuum," *Nature* **541**, 196–199 (2017).
8. J. H. Yang et al., "Low-threshold bound state in the continuum lasers in hybrid lattice resonance metasurfaces," *Laser Photonics Rev.* **15**, 2100118 (2021).

9. M. Wu et al., "Room-temperature lasing in colloidal nanoplatelets via Mie-resonant bound states in the continuum," *Nano Lett.* **20**, 6005–6011 (2020).
10. M. Wu et al., "Bound state in the continuum in nanoantenna-coupled slab waveguide enables low-threshold quantum-dot lasing," *Nano Lett.* **21**, 9754–9760 (2021).
11. S. Joseph et al., "Bound states in the continuum in resonant nanostructures: an overview of engineered materials for tailored applications," *Nanophotonics* **10**, 4175–4207 (2021).
12. C. Kittel, *Introduction to Solid State Physics*, Wiley (2004).
13. J. M. Foley, S. M. Young, and J. D. Phillips, "Symmetry-protected mode coupling near normal incidence for narrow-band transmission filtering in a dielectric grating," *Phys. Rev. B* **89**, 165111 (2014).
14. Y. Wang et al., "Highly controllable etchless perovskite microlasers based on bound states in the continuum," *ACS Nano* **15**, 7386–7391 (2021).
15. S. I. Azzam et al., "Formation of bound states in the continuum in hybrid plasmonic-photonic systems," *Phys. Rev. Lett.* **121**, 253901 (2018).
16. R. Kikkawa, M. Nishida, and Y. Kadoya, "Polarization-based branch selection of bound states in the continuum in dielectric waveguide modes anti-crossed by a metal grating," *New J. Phys.* **21**, 113020 (2019).
17. C. M. Bender, *PT Symmetry: In Quantum and Classical Physics*, World Scientific Publishing (2018).
18. S. T. Ha et al., "Directional lasing in resonant semiconductor nanoantenna arrays," *Nat. Nanotechnol.* **13**, 1042–1047 (2018).
19. S. I. Azzam et al., "Single and multi-mode directional lasing from arrays of dielectric nanoresonators," *Laser Photonics Rev.* **15**, 2000411 (2021).
20. M. S. Hwang et al., "Ultralow-threshold laser using super-bound states in the continuum," *Nat. Commun.* **12**, 4135 (2021).
21. C. W. Hsu et al., "Observation of trapped light within the radiation continuum," *Nature* **499**, 188–191 (2013).
22. X. Gao et al., "Formation mechanism of guided resonances and bound states in the continuum in photonic crystal slabs," *Sci. Rep.* **6**, 31908 (2016).
23. E. N. Bulgakov and D. N. Maksimov, "Avoided crossings and bound states in the continuum in low-contrast dielectric gratings," *Phys. Rev. A* **98**, 053840 (2018).
24. M. R. Hashemi et al., "Electronically-controlled beam-steering through vanadium dioxide metasurfaces," *Sci. Rep.* **6**, 35439 (2016).
25. P. C. Wu et al., "Dynamic beam steering with all-dielectric electro-optic III-V multiple-quantum-well metasurfaces," *Nat. Commun.* **10**, 3654 (2019).
26. P. Thureja et al., "Array-level inverse design of beam steering active metasurfaces," *ACS Nano* **14**, 15042–15055 (2020).
27. Z. Li et al., "Actively switchable beam-steering via hydrophilic/hydrophobic-selective design of water-immersed metasurface," *Adv. Opt. Mater.* **9**, 2100297 (2021).



**Zhen-Ting Huang** received his PhD from the Department of Photonics at National Yang Ming Chiao Tung University. His research interest is surface plasmon polariton nanolasers.

**Chiao-Yun Chang** received her MS degree from the Department of Photonics at National Yang Ming Chiao Tung University. Her research interest is surface plasmon polariton nanolasers.

**Kuo-Ping Chen** received his PhD in electrical and computer engineering from Purdue University in 2011. He is a professor at the Institute of Photonics Technologies, National Tsing Hua University. His research interests are in nanophotonics and metamaterials, which include nanofabrication, plasmonics, sensors, nanoantennas, and metasurfaces. He was honored with the MOST Ta-You Wu Memorial Award and the 19th Y. Z. Hsu Scientific Paper Award in 2021.

**Tien-Chang Lu** is Distinguished Professor in the Department of Photonics, National Yang Ming Chiao Tung University. He has broad research interests including surface plasmon polariton nanolasers, photonic-crystal surface-emitting lasers, and vertical-cavity surface-emitting lasers. He is an OPTICA Fellow, SPIE Fellow, and IEEE Senior Member.